



Corrosion behaviors of W-doped laser-cladded high-entropy alloy of AlCoCrFeNi in a simulated sulfur-containing seawater environment

Yang Zhao ^a, Zhikai Zhu ^a, Wenqing Shi ^b, Jiang Huang ^{a,*}

^a School of Electronics and Information Engineering, Guangdong Ocean University, Zhanjiang, 524088, China

^b School of Materials Science and Engineering, Guangdong Ocean University, Yangjiang, 529500, China

ARTICLE INFO

Keywords:

AlCoCrFeNi
W-doping
Localized corrosion
Simulated sulfur-containing seawater

ABSTRACT

The localized corrosion in a simulated seawater environment is related to sulfide, and few studies have investigated the corrosion behaviors of laser-cladded AlCoCrFeNi high-entropy alloy (HEA) systems in a simulated sulfur-containing seawater environment. Corrosion behaviors of HEA/W_x ($x = 0, 5$, and 15 wt%) coatings have been worked out by potentiodynamic polarization, electrochemical impedance spectroscopy (EIS), Mott-Schottky analysis, X-ray photoelectron spectroscopy (XPS) analysis, and immersion corrosion tests. W-doped HEA coatings can change the ratio of A2 to B2 phases and affect the corrosion resistance. The potentiodynamic polarization and EIS results reveal that a small quantity of W-doped (5 wt%) HEA coatings form a denser passivation film that is particularly resistant to localized corrosion. By analyzing the corrosion behaviors of the HEA/W_x coatings, it was determined that a small amount of W-doped (5 wt%) HEA coatings had better localized and improved corrosion resistance. However, excessively W-doped (15 wt%) HEA coatings have reduced corrosion resistance. The Mott-Schottky analysis revealed that the HEA/W_x coatings ($x = 0, 5$, and 15 wt%) have the property of P-N-type semiconductors. XPS analysis was used to analyze the film composition. The results demonstrated that the passivation film combined Cr₂O₃, Al₂O₃, Fe₂O₃, and WO₃. Based on the immersion corrosion test, localized corrosion types were mainly intergranular and crevice.

1. Introduction

Chloride is expected in the marine environment and serves as a promoter for metal corrosion, which is harmful to metals and may cause the breakdown of the metal surface passivation film [1]. Sulfides exist in marine ecosystems and have been mainly generated by the conversion of SO₂ or H₂S produced by eruptions and explosions [2–4]. Metabolites of organisms and bacteria in the oceans play a role in the formation of biogenic sulfide [5]. Previous studies [6] have shown that sulfate-reducing bacteria metabolize thiosulfate to create zero-valent sulfur. Marko et al. [7] investigated carbon steel corrosion in a saltwater environment with sulfate-reducing bacteria. After long-term interaction between sulfate-reducing bacteria and metal in seawater, it was found that the products of SRB metabolism and H₂S react to form Fe_xS_y on the metal surface. The passivation film was damaged in a simulated sulfur-containing saltwater environment while sulfides and chlorides were adsorbed on the material's surface [8]. Chloride and sulfur ions react with alloy coatings to form chlorides and sulfides, which are adsorbed on the surface of the layer to prevent the repair of

the passivation film on the surface of alloy coatings in a simulated sulfur-containing seawater environment, leading to localized corrosion [9,10]. Local corrosion is mainly pitting corrosion, intergranular corrosion (IGC), corrosion fatigue, crevice corrosion, and intergranular corrosion, which harm the metal surface [10–12]. In 2004, Yeh and Cantor et al. [13,14] found a high-entropy alloy that was made up of more than four master alloy elements whose mixed entropy had a higher value than 1.5 R (where R represents the gas constant 8.314 J K⁻¹ • mol⁻¹) [15,16]. AlCoCrFeNi high-entropy alloy (HEA) with body-centred cubic (BCC) structures has attracted more attention because of its advantageous features [17]. Researchers studying high-entropy alloys (HEA) can examine the BCC type in both the Fe-Cr-rich disordered body-centred cubic (A2) phase and the Al-Ni-rich ordered body-centred cubic (B2) phase [18]. HEA has the same advantages of corrosion resistance as well as high strength as common single-master alloys, which are frequently used in sea engineering equipment [19,20]. However, HEA is costly to manufacture using typical alloys, which limits its widespread practicality [21,22]. The laser cladding method provides advantages in the form of minimum

* Corresponding author.

E-mail address: huangjiang@gdou.edu.cn (J. Huang).

pollution, a simple process, a wide selection of substances, a low diluted pace, and strong bonding capacity [23–25]. Therefore, HEA was established using the laser cladding technique to decrease the cost and improve surface performance [26–28]. Recent studies indicate that insoluble metallic elements (Mo, Nb, Ta, W, and Zr) have a significant impact on the corrosion resistance of high-entropy alloys [29–32]. Li et al. [33] found that the passivation film was stabilized by forming a single-phase BCC structure with a uniform elemental distribution and by enriching Cr³⁺, Al³⁺, and Ti⁴⁺. The TiCrVNb_{0.5}Al_{0.5} alloys exhibit lower corrosion current densities, higher breakdown potentials, and excellent re-passivation capabilities than conventional alloys in 3.5 wt% NaCl and 1 M HCl solutions. Wang et al. [34] revealed that raising the Mo element produces a diminution in B2 phase content and an increase in Cr-rich and Mo-rich oxides in the passivation film, culminating in enhanced resistance to corrosion of the passivation film in 3.5 wt% NaCl solution. Zhou et al. [35] observed that during the corrosion process of FeCo-NiCrMnW_x in 3.5 wt% NaCl solution, the W element acts as an anti-cathode, and Fe, Mn, and Cr act as cathodes. While the passivation film breaks, the W particles convert into W³⁺ and enter the solution, which leads to selective disintegration around the W element. Niu et al. [36] discovered that including tungsten in high-entropy alloys (HEAs) enhanced resistance to pitting in saltwater solutions. Of these alloys, CoCrFeNiW_{0.5} exhibits superior pitting resistance and excellent passivation stability.

Few studies have been done regarding the corrosion behaviors of the W-doped AlCoCrFeNi high-entropy alloy in a simulated sulfur-containing seawater environment. In our studies, HEA/W_x ($x = 0, 5$, and 15 wt%) coatings were produced on 316L stainless steel by the laser cladding method. Corrosion behaviors of HEA/W_x ($x = 0, 5$, and 15 wt %) coatings have been investigated in a simulated sulfur-containing saltwater environment.

2. Experiment

2.1. Materials

The rules for the 316L stainless steel substrate were $100 \times 50 \times 3$ mm². The chemical composition of the 316L substrate appears in Table 1. The cladding material used was AlCoCrFeNi high-entropy alloy (HEA) powder, having an average diameter of 50–90 μm . Table 1 describes the chemical structure of HEA. Tungsten (W) powder with typical diameters of 53–150 μm as the hard phase has been added to the HEA powder to produce HEA/W_x coatings (x : mass fraction ratio; $x = 0, 5$, and 15 %), which could be made by 0 wt%, 5 wt%, and 15 wt% specimens. The mixture was homogenized for an hour.

2.2. Laser cladding process

Laser cladding coatings were melted by a laser cladding system (Model XL-F2000T; maximum power output: 2000 W; laser beam wavelength: 1080 ± 5 nm). The laser cladding system (Model XL-F2000T) has been employed to melt coatings with a maximum power output of 2000 W and a laser beam wavelength of 1080 ± 5 nm. The laser power was 1200 W, the scanning speed was 600/min, the defocus amount was +2 mm, and the spot diameter was 3 mm. After polishing the 316L substrate, we thoroughly dried it with 100 % ethanol. Laser cladding creates 1 mm-thick cladding powder on 316L stainless steel. The cutter could divide the generated specimens into 10×10 mm². The cross-section has been studied using a scanning electron microscope

(model: Quanta 250 FEG, produced by FEI Company, Hillsborough, OR, USA), an energy dispersive spectrometer (EDS), and point scanning technology (EDX) to investigate its microscopic organization. The outermost layer was subjected to electrochemical and immersion experiments to assess its corrosion resistance. The laser layer's phase composition was studied using X-ray diffraction equipment (XRD-6100, Shimadzu, Shimane-ken, Japan) at a scanning speed of 6°/min and a diffraction angle that extended from 20° to 90°. Microhardness measurements of the cladding and substrate were performed using a Vickers hardness tester (Model: MHVD-1000AT, Manufacturer: Yizong Precision Instrument Co., Ltd., Shanghai, China) at a load of 200 g for 10 s.

2.3. Performance test

2.3.1. Electrochemical test

Different types of corrosion agents are used to look at potentiodynamic polarization curves and electrochemical impedance spectra (EIS). These are a 3.5 wt%/L NaCl solution with a pH of 7 and a 3.5 wt%/L NaCl plus 0.002 mol/L Na₂O₃ solution with a pH of 6.8. An electrochemical workstation (CHI660E, Chen Hua Instruments, Shanghai, China) has been used to assess corrosion resistance. The conventional three-electrode setup was used, with the specimen as the working electrode, the platinum sheet as the auxiliary electrode, and the saturated calomel electrode (SCE) as the reference electrode. Before testing, insulation adhesive had been used to secure the regions other than the coating. The Mott-Schottky curve was scanned from -0.6 V to 0.6 V with 0.5 V/s at a frequency of 1000 Hz in 3.5 wt%/L NaCl plus 0.002 mol/L Na₂O₃ solution.

2.3.2. XPS analysis

The samples were submerged for 10 h in a 3.5 wt%/L NaCl plus 0.002 mol/L Na₂O₃ solution. Continuous potential polarization was applied at 0.5 eV for 6000 s. After being washed and dried with ethanol, the test samples were put on a sample tray. The sample chamber was filled with the prepared samples and allowed to evacuate to reach the necessary vacuum level, which is usually less than 2.0×10^{-7} mbar. X-ray photoelectron spectroscopy (XPS) (Thermo Kalpha; Thermo ESCALAB 250XI; Axis Ultra DLD Kratos AXIS SUPRA; PHI-5000 Versaprobe III) was used to figure out the type of passivation film that was on the specimen's surface.

2.3.3. Immersion corrosion experiment

The immersion corrosion experiment was designed to illustrate the corrosion behavior induced by chemical corrosion. Before the immersion corrosion experiment, the microstructure of the specimens was inspected using an optical microscope (OM) (model: Ario Imager M2m, Zeiss, Germany). The specimens were placed with corrosion-resistant wire and sticks in 1L beakers. Pure water had been treated with 3.5 wt%/L NaCl and 0.002 mol/L Na₂O₃ solutions (PH = 6.8). To monitor the chemical corrosion of the specimens in the solution, they were suspended vertically in a beaker of chloride solution containing thiosulfate for 1000 h in a closed environment. The specimens were put in an ultrasonic cleaner containing a dilute hydrochloric acid solution and heated to 60 °C for 10 min. The specimens were then rinsed with anhydrous ethanol before drying. The corrosion morphology was investigated with a scanning electron microscope (SEM), and the corrosion products were assessed using line scanning technology (EDX).

Table 1

Chemical composition of the AlCoCrFeNi high-entropy alloy and the 316L stainless steel (mass fraction, %.).

Material	Al	Co	Cr	Fe	Ni	Mn	Mo	Si
AlCoCrFeNi	11.09	23.34	20.19	21.72	23.53	/	/	/
316L	/	/	16–18	Bal	10–14	2	2–3	1.5

3. Results

3.1. Phase composition

The XRD patterns of the HEA/W_x (x = 0, 5, and 15 wt%) specimens are displayed in Fig. 1. The three most significant diffraction peaks of HEA coatings in X-ray diffraction patterns are recognized as the typical peaks of ordered body-centred cubic (B2) and disordered body-centred cubic (A2) phases. Previous studies [37,38] discovered that in the HEA coating, Al elements exist mainly as the Al–Ni-rich B2 phase, whereas Cr elements exist primarily as the Fe–Cr-rich A2 phase. A new diffraction peak for the 15 wt% specimen regarding the W phase was discovered at 40.15°. The A2/B2 phases coexisted, and the A2 peaks increased as the W increased. The enlarged peak for the 15 wt% specimen changes to a tiny angle of 0.2°, with a 20 range of 42–48° (see Fig. 1 (b)). The diffraction peaks shift leftward, indicating that the 15 wt% W-doped HEA coating induces lattice deformation.

The cross-sectional area of 5 wt% and 15 wt% specimens completed EDX point analysis at various sites, as shown in Fig. 2. The distribution elements at multiple sites indicate that the Al and Ni components follow the same pattern, and the Cr and Fe elements show a similar pattern in the 15 wt% specimen. It suggests that the Fe–Cr-rich A2 phase and Al–Ni-rich B2 phase continue to develop when W content is added. The increase in W content from 5 wt% to 15 wt% is associated with a drop in Al and Ni content, indicating that the 15 wt% W-doped HEA coating reduces the fraction of the B2 phase. According to the formula in Eq. (1) [39],

$$\Delta S_{mix} = -R \sum_{i=1}^n C_i \ln i \quad (1)$$

R is the gas constant ($8.314 \text{ J}\cdot\text{K}^{-1} \text{ mol}^{-1}$). C_i is the atomic fraction. The mixed entropy (ΔS_{mix}) value of AlCoCrFeNi is 1.6 R. By applying EDX point analysis and ΔS_{mix} values (refer to Table 2), the average ΔS_{mix} value of the 5 wt% specimen decreases to 1.58 R. However, with the 15 wt% W-doped HEA coating, the ΔS_{mix} value returns to 1.6 R. It demonstrates that W-doped HEA coatings still fall within the HEA category. The ΔS_{mix} value of a high-entropy alloy is determined by combining the ΔS_{mix} values of the individual components or compounds. Manipulating the elements allows for modification of the ΔS_{mix} value. HEA has no solutes or solvents. A small quantity of W-doped in the HEA coating operates as a solvent. It eliminates eliminates the ΔS_{mix} value, but as the W-doped in the HEA coating increases, the more complicated the internal structure of the alloy, the higher the ΔS_{mix} value [14,16]. Fig. 3 depicts the EDS elemental mapping study of cross-sectional microstructures. The 15 wt% specimen is not evenly distributed (see Fig. 3 (h))

and is deposited in the bottom area of the cladding. The W element mixes partially with Co, Ni, and Al elements (see Fig. 3 (c, b, g)) to create the spherical W-rich phase. The enrichment of the W element at the bottom during the melting and cladding process is caused by the effect of convection in the melt pool at high temperatures, where the W element is evenly distributed and suspended in the molten coating. At the same time, due to the high density, the W-rich phase moves to the bottom under the gravity factor [40].

The cross-sectional area of HEA/W_x (x = 0, 5, and 15 wt%) specimens reveals thick, uniform coatings with appropriate metallurgical interaction with the substrate, as shown in Fig. 4. The cross-sectional microstructure of the coatings has been separated into two distinct regions: the top part (see Fig. 4(a–b)) shows equiaxed crystal morphology. At the same time, Fig. 4 (c) suggests bulk crystals. The bottom parts of the 0 wt% and 5 wt% specimens (see Fig. 4(b–e)) are dominated by blocky crystals, while the 15 wt% specimen (see Fig. 4 (f)) possesses columnar crystals primarily. According to the EDX point analysis (see Table 2), the decrease in Al–Ni content in the 15 wt% specimen indicates that the decline in the Al–Ni-rich B2 phase and the 15 wt% W-doped HEA coating may be responsible for the decrease in cooling rate R and the increase in temperature gradient G. The crystal structure is related to the ratio of G/R [41]. G is the temperature gradient. R is the cooling rate. The 15 wt% W-doped HEA coating might lower the R and raise the G, allowing the change from bulk crystals to columnar crystals at the bottom region and from equiaxed bulk crystals to bulk crystals at the upper region. Li et al. [42] revealed that decreasing the elemental quantity of aluminium in the Al_xCoCrFeNi alloy causes it to shift from equiaxed crystals to block crystals while boosting grain size.

3.2. Microhardness

Fig. 5(a) shows a schematic of the microhardness distribution of HEA/W_x (x = 0, 5, and 15 wt%) specimens. The average microhardness of 0 wt%, 5 wt%, and 15 wt% specimens was 531.85, 536.79, and 541.67 (HV_{0.2}), respectively. Fig. 5(b–c) shows a schematic of the indentation of a spherical W-rich particle in the bottom region. The microhardness of the W-rich particles found in the 5 wt% specimen was 342.5 (HV_{0.2}), with a diameter of 29.52 μm (see Fig. 5(c)). The microhardness of the W-rich particles of the 15 wt% specimen was 393.3 (HV_{0.2}) with a diameter of 26.53 μm (see Fig. 5(b)). W-rich particles have a much lower microhardness than coatings. However, as the W element concentration increases, the indentation size reduces, enhancing the microhardness, which is lower than coatings. Furthermore, the W element establishes a slight improvement in the microhardness of coatings.

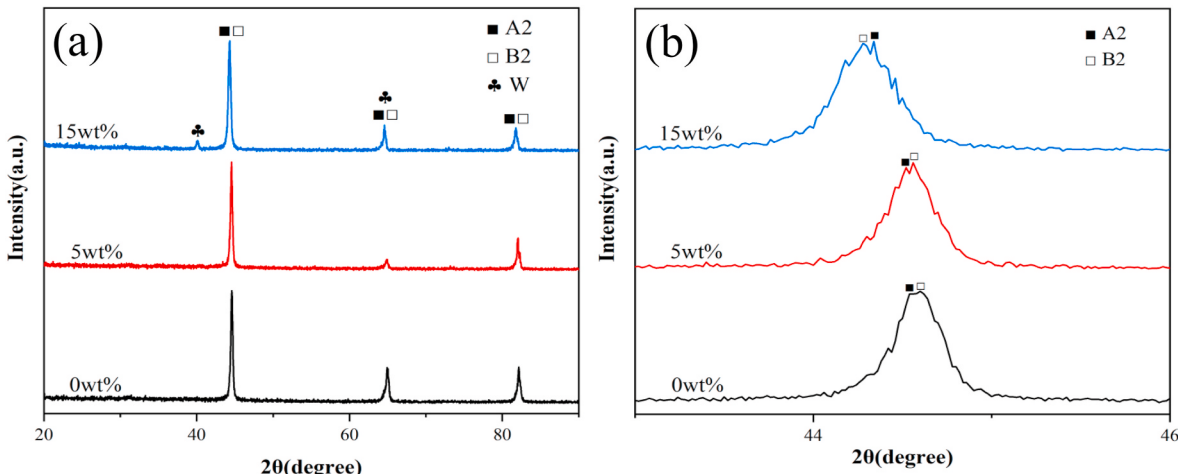


Fig. 1. The XRD patterns of the HEA/W_x (x = 0, 5, and 15 wt%) specimens.

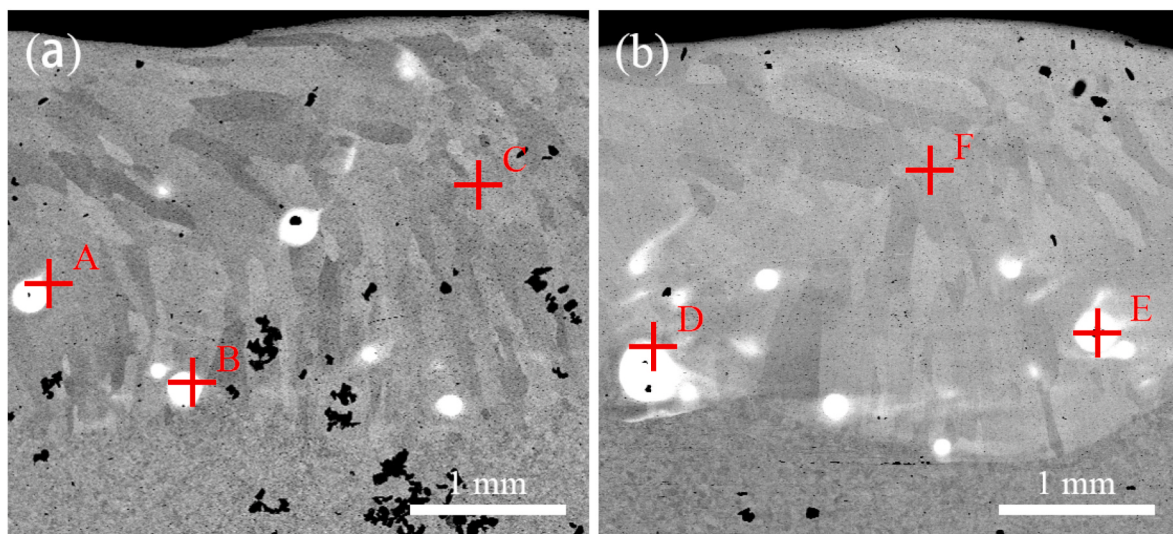


Fig. 2. Positions of EDX points for 5 wt% and 15 wt% specimens. (a) 5 wt% specimen; (b) 15 wt% specimen.

Table 2
EDX point analysis of 5 wt% and 15 wt% specimens.

Region	Element (at. %)						ΔS_{mix}
	Al	Cr	Fe	Co	Ni	W	
A	12.70	19.88	35.03	14.90	16.54	0.95	1.58R
B	12.31	20.22	35.60	14.29	16.34	1.25	1.56R
C	14.59	20.55	33.55	14.55	15.51	1.26	1.60R
D	10.90	20.42	37.21	13.33	15.61	2.52	1.59R
E	11.39	19.92	36.02	14.06	15.57	3.03	1.61R
F	10.88	20.62	36.70	13.71	15.46	2.64	1.59 R

3.3. Potentiodynamic polarization curve analysis

The potentiodynamic polarization curves of all specimens were examined in 3.5 wt%/L NaCl solution and 3.5 wt%/L NaCl plus 0.002 mol/L Na₂O₃ solutions, which are displayed in Fig. 6. The electrochemical parameters gained from polarization curves (see Fig. 6) are listed in Table 3. Five electrochemical parameters were used to assess the corrosion resistance of coatings where passivation zones appeared apparent in the polarization curve: self-corrosion potential (E_{corr}), corrosion current density (i_{corr}), initiating passive potential (E_p), passive current density (i_p), and breakdown potential (E_b). Self-corrosion potential (E_{corr}) is the tendency of the coating surface to corrode. On the laser cladding surface, the corrosion current density (i_{corr}) was known as the corrosion ratio.

Passive current density (i_p) was considered to form the corrosion rate of the stable passivation zone. A lower passive current density indicates a lower passivation dissolution rate. Breakdown potential (E_b) is the potential at which the passivation film is broken. A higher E_b value indicates more excellent resistance to localized corrosion. When current density changes slowly with the addition of electrode potential, the surface of coatings generates a passivation film, known as initiating passive potential (E_p). According to the electrochemical parameters in Table 3, the good corrosive properties of the coatings can be demonstrated by a higher self-corrosion potential (E_{corr}), lower corrosion current density (i_{corr}), and lower passivation current density (i_p) [43]. Therefore, the 5 wt% specimen in 3.5 wt%/L NaCl and 3.5 wt%/L NaCl plus 0.002 mol/L Na₂O₃ solutions have a higher E_{corr} , i_{corr} , and i_p value, which shows that the 5 wt% W-doped HEA coating retards the dissolution rate of passive film, the corrosion rate of coating, corrosion tendency, and localized corrosion generation. It can be seen from Fig. 6(a) that the breakdown potential (E_b) of the HEA/W_x ($x = 0, 5$, and 15 wt%) specimens in 3.5 wt%/L NaCl solution is higher than that of the 316L

substrate. The E_b value of the 316L substrate is dropped to less than that of the HEA/W_x specimens after the 0.002 mol/L Na₂O₃ solution has been introduced to the 3.5 wt%/L NaCl solution (see Fig. 6(b)). It suggested that the 316L substrate is more resistant to local corrosion than W-doped HEA coatings in 3.5 wt%/L NaCl plus 0.002 mol/L Na₂O₃ solution. Because of a small amount of Mo in the 316L substrate, Mo and oxygen elements in the passivation process generate MoO₂ and MoO₃, which play a role in repairing the passivation film, preventing passivation film rupture and pitting corrosion [32]. By doping the HEA coating with the W element, the E_b value of all specimens revealed increasing and subsequently diminishing patterns. The 5 wt% specimen indicates greater E_b values than other specimens, which suggests the 5 wt% W-doped HEA coating is more resistant to local corrosion. Fig. 6 shows the passivation region of the anodic polarization process for the 316L substrate and HEA/W_x ($x = 0, 5$, and 15 wt%) specimens in 3.5 wt%/L NaCl and 3.5 wt%/L NaCl plus 0.002 mol/L Na₂O₃ solutions. The passivation region that exists between E_p and E_b potentials showed an activation-passive transition region (II) and a stable passivation region (I) in the anodic area of the polarization curves [44]. A stable rate of current density changes with the addition of potential characterizes the stable passivation region (I). The activation-passive transition (II) shows a slow current density rate increases with unstable fluctuations. A rapid growth in current density in the anodic polarization process over E_b potential indicates local corrosion [45].

Referring to the immersion corrosion experiment, due to the cracks created by the W addition in HEA coatings (see Fig. 12), the adsorption of sulfur ions into the cracks and crevices further accelerates the generation of localized corrosion [46]. The chloride ions decompose the passivation film, whereas chloride and sulfur ions interact, and thiosulfate reduces sulfur to adsorption on the metal surface. Chloride and sulfur may compete for adsorption, exacerbating the degradation of the passivation film [47]. While thiosulfate is present, the dissolving rate rises, impairing the passive film's protective properties.

3.4. EIS analysis

The electrochemical impedance spectra (EIS) method was developed to analyze the passivation film on the coating surface better. The 316L substrate and HEA/W_x ($x = 0, 5$, and 15 wt%) specimens in 3.5 wt%/L NaCl and 3.5 wt%/L NaCl plus 0.002 mol/L Na₂O₃ solutions are displayed in Nyquist plots, as shown in Fig. 7. The capacitance loop radius (see Fig. 7) represents the interfacial resistance to charge transfer, which is typically linked to charge transfer at the electrode or electrolyte interface and the passivation film formed by the passivation of the

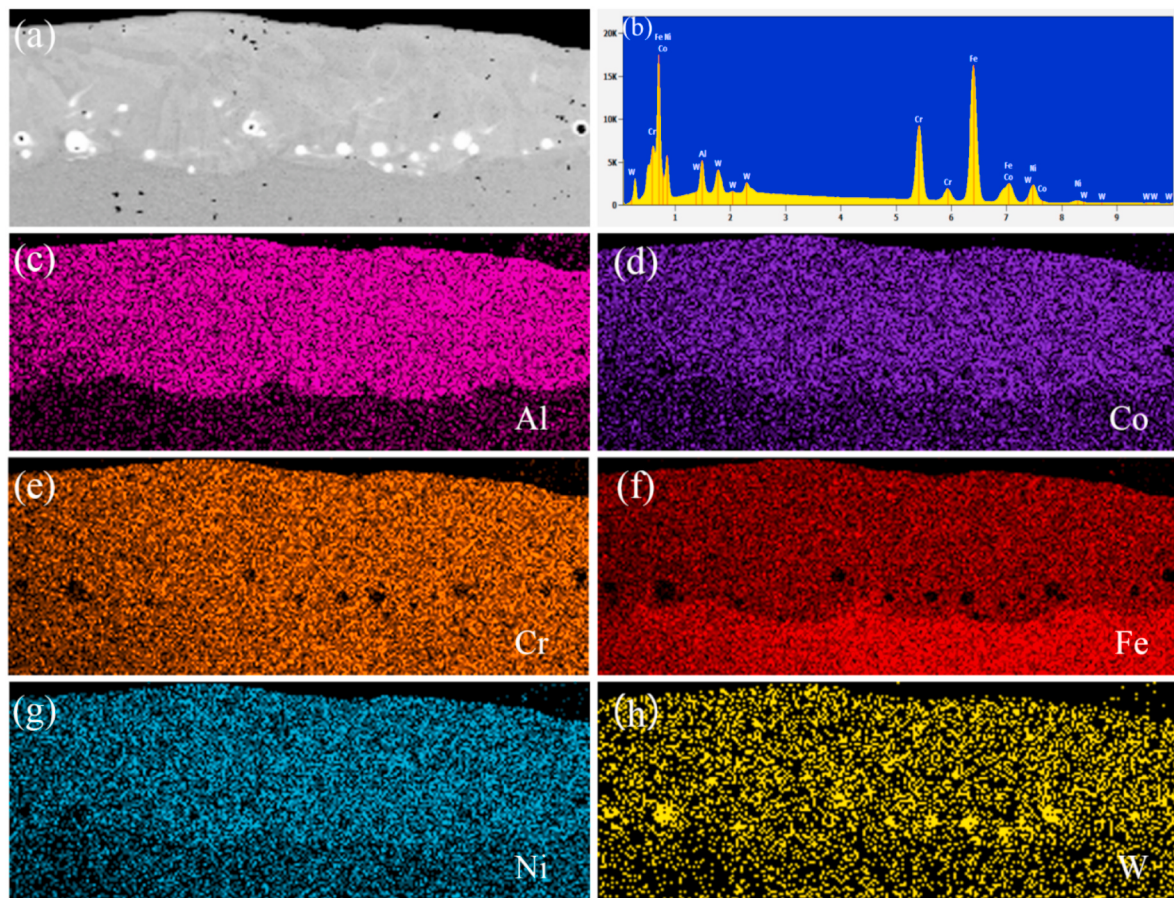


Fig. 3. EDS elemental mapping analysis of cross-section microstructures.

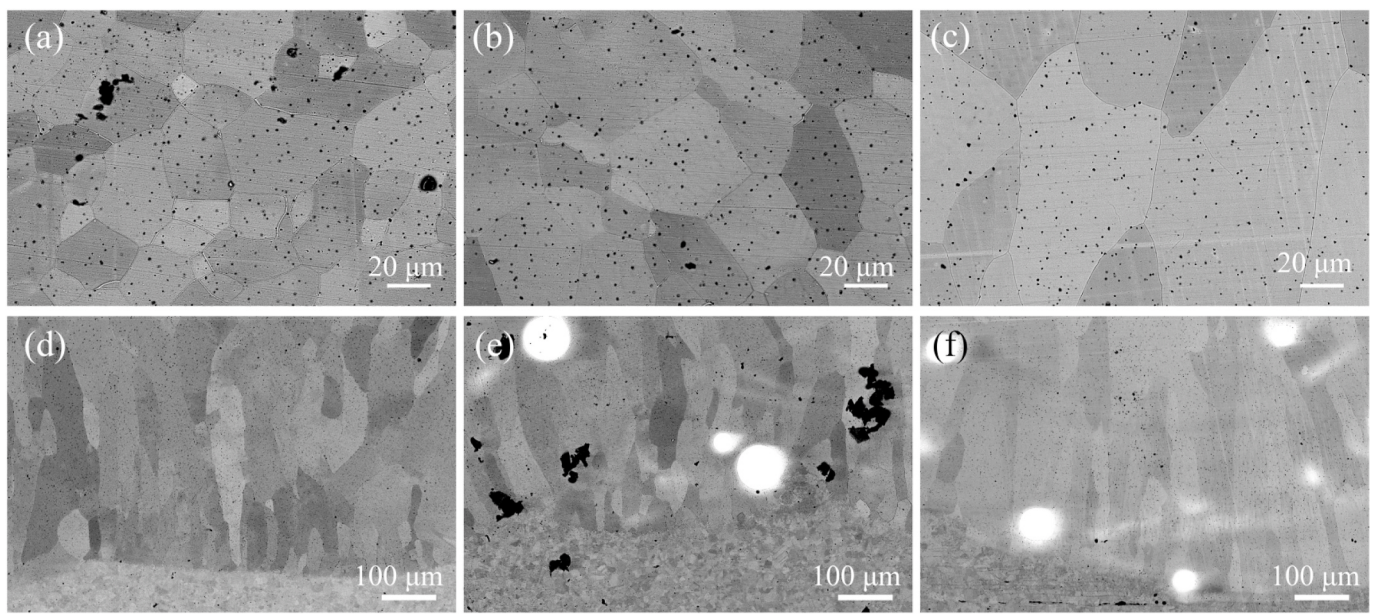


Fig. 4. (a–c) are the cross-sectional microstructure of 0 wt%, 5 wt%, and 15 wt% specimens in the up region; (d–f) are the cross-sectional microstructure of 0 wt%, 5 wt%, and 15 wt% specimens in the bottom region.

coating surface [48]. In general, specimens with a larger capacitive loop radius have better corrosion resistance. The sorted capacitive cyclic radius for HEA/W_x specimens in 3.5 wt%/L NaCl and 3.5 wt%/L NaCl plus 0.002 mol/L Na₂O₃ solutions is 5 wt% specimen >15 wt%

specimen >0 wt% specimen >316L substrate. The 5 wt% specimen has a greater capacitive loop radius, which possesses superior corrosion resistance in 3.5 wt%/L NaCl and 3.5 wt%/L NaCl plus 0.002 mol/L Na₂O₃ solutions.

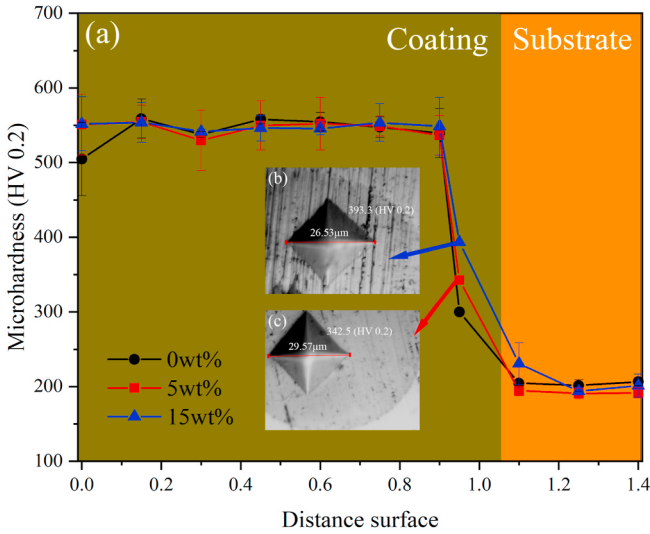


Fig. 5. The schematics of the microhardness distribution and indentation of the HEA/W_x ($x = 0, 5$, and 15 wt%) specimens; (a) The microhardness distribution of HEA/W_x ($x = 0, 5$, and 15 wt%) specimens; (b) and (c) are the schematics of microhardness indentation of spherical W particles of the 15 wt% and 5 wt% specimens.

In Bode plots, as shown in Fig. 8, the negative phase angle of HEA/W_x specimens in 3.5 wt%/L NaCl solution is around 75° , while the negative phase angle of 316L substrate is 68.1° . However, the 316L substrate, 5 wt% specimen, and 15 wt% specimen in 3.5 wt%/L NaCl plus 0.002 mol/L Na₂S₂O₃ solution keep right below 70° , and the 5 wt% specimen reaches up to 74.9° . As a result, a higher negative phase angle indicated that a denser passivation film was formed on the metal surface. The negative phase angle was compared between the 316L substrate and HEA/W_x specimens, indicating that the 5 wt% specimen exhibits a denser passivation film. In addition, the higher transfer resistance (R_{ct}) of the specimens can be characterized by the higher impedance modulus $|Z|$ (see Fig. 8) in the low-frequency region (10^{-1} – 10^0), meaning a more densely passivation film [49,50]. The degree of $|Z|$ in 3.5 wt%/L NaCl and 3.5 wt%/L NaCl plus 0.002 mol/L Na₂S₂O₃ solutions was in the range of 5 wt% specimen > 15 wt% specimen > 0 wt% specimen > 316L substrate (see Table 4), which seems consistent with the results for the capacitance ring radius. The results show that the denser passivation film of HEA/W_x specimens is higher than that of 316L substrate in 3.5 wt%

%/L NaCl and 3.5 wt%/L NaCl plus 0.002 mol/L Na₂S₂O₃ solutions. The 5 wt% specimen has a denser passivation film than the others.

Fig. 9 shows the equivalent circuit of the EIS diagram, and the fitting results are shown in Table 4. In the equivalent circuit, R_s denotes the chloride solution's resistance to thiosulfate. R_f denotes the passivation film's resistance to the specimen's surface. Q_f is the capacitance between the solution and the passivation film. R_{ct} is the transfer resistance between the surface of the specimen and solution after the passivation film is damaged, and Q_{dl} is the electric double-layer capacitance. The dispersion coefficients Q_{n1} and n_2 are given. When the n value approaches 1, a higher density of passivation film forms on the metal surface.

Table 4 shows the equivalent circuit parameters of the electrochemical impedance spectrum. The passivation film's polarization resistance (R_p) is its surface resistance. A higher polarization resistance indicates superior corrosion resistance. The polarization impedance of the specimen in chloride solution and chloride solution with thiosulfate can be calculated using the formula in Eq. (2) [49].

$$R_p = R_s + R_f + R_{ct} \quad (2)$$

The polarization resistance of the 316L substrate and HEA/W_x ($x = 0, 5$, and 15 wt%) specimens in 3.5 wt%/L NaCl and 3.5 wt%/L NaCl plus

Table 3

Electrochemical parameters of the 316L substrate and HEA/W_x ($x = 0, 5$, and 15 wt%) specimens in 3.5 wt%/L NaCl and 3.5 wt%/L NaCl plus 0.002 mol/L Na₂S₂O₃ solutions.

	Solution	E_{corr}/V_{SCE}	$i_{corr}/A/cm^2$	E_{ip}/V_{SCE}	$i_p/A/cm^2$	E_b/V_{SCE}
316L	3.5 wt%/L NaCl	-0.920	1.121×10^{-7}	-0.712	3.951×10^{-5}	0.085
0 wt %		-0.916	4.477×10^{-8}	-0.828	1.777×10^{-5}	0.075
5 wt %		-0.881	-4.091×10^{-9}	-0.804	1.499×10^{-5}	0.148
15 wt %		-0.889	2.080×10^{-8}	-0.793	5.478×10^{-5}	0.127
316L	3.5 wt%/L NaCl	-0.945	3.217×10^{-7}	-0.844	5.275×10^{-5}	0.096
0 wt %	Plus 0.002 mol/L Na ₂ S ₂ O ₃	-0.960	-2.161×10^{-7}	-8.55	4.375×10^{-5}	-0.142
5 wt %		-0.896	-2.530×10^{-7}	-0.777	1.936×10^{-5}	-0.062
15 wt %		-0.930	-2.314×10^{-7}	-0.803	3.923×10^{-5}	-0.103

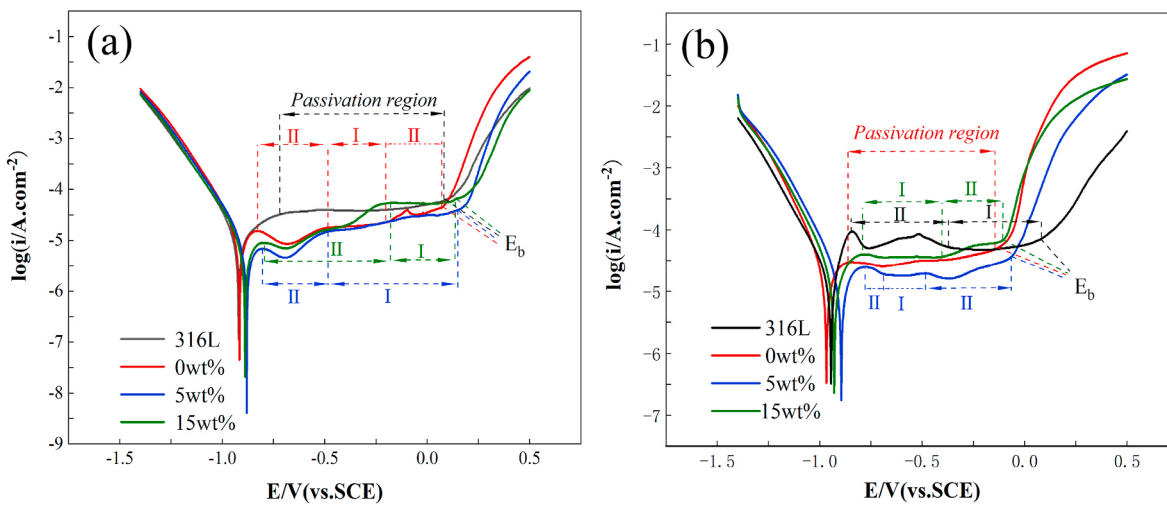


Fig. 6. Potentiodynamic polarization curves of the 316L substrate and HEA/W_x ($x = 0, 5$, and 15 wt%) specimens. (a) 3.5 wt%/L NaCl solution; (b) 3.5 wt%/L NaCl plus 0.002 mol/L Na₂S₂O₃ solution.

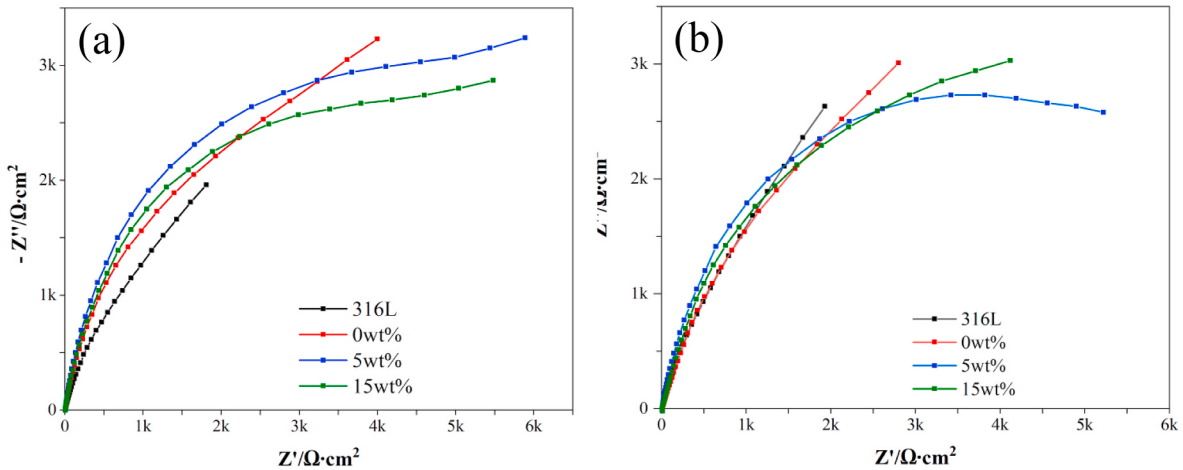


Fig. 7. The Nyquist plots for 316L substrate and HEA/ W_x ($x = 0, 5$, and 15 wt%) specimens. (a) 3.5 wt%/L NaCl solution; (b) 3.5 wt%/L NaCl plus 0.002 mol/L Na₂S₂O₃ solution.

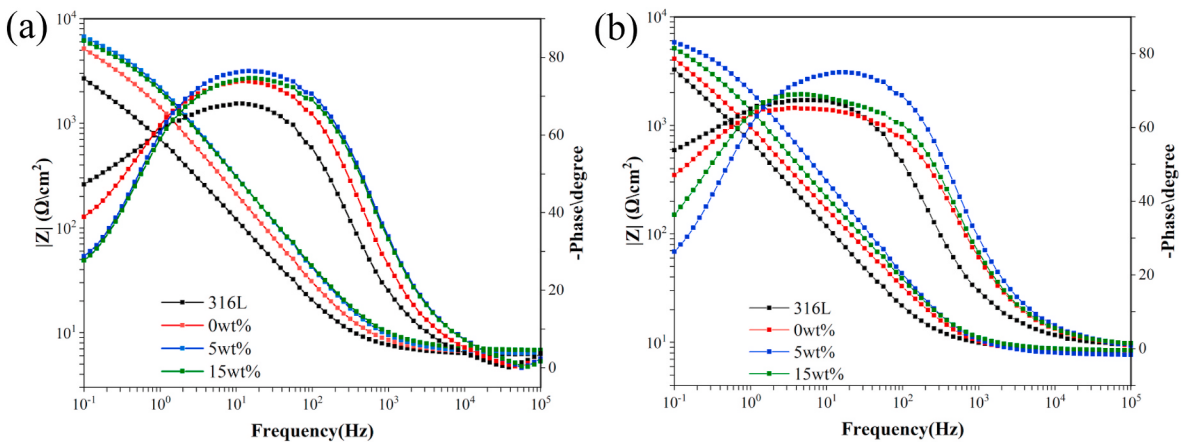


Fig. 8. The Bode plots for 316L substrate and HEA/ W_x ($x = 0, 5$, and 15 wt%) specimens. (a) 3.5 wt%/L NaCl solution; (b) 3.5 wt%/L NaCl plus 0.002 mol/L Na₂S₂O₃ solution.

Table 4
Equivalent circuit parameters of the electrochemical impedance spectrum.

Specimen	Solution	$R_S/(\Omega \cdot \text{cm}^2)$	$R_f/(\Omega \cdot \text{cm}^2)$	$Q_f \cdot Y_0 (\Omega^{-1} \text{cm}^{-2} \cdot s^n)$	$Q \cdot n_1$	$Q_{dl} \cdot Y_0 (\Omega^{-1} \text{cm}^{-2} \cdot s^n)$	$Q \cdot n_2$	$R_{ct}/(\Omega \cdot \text{cm}^2)$	$R_p/(\Omega \cdot \text{cm}^2)$
316L	Chloride	6.315	2224	2.780×10^{-4}	0.823	3.125×10^{-4}	0.789	3877	6.107×10^3
0 wt%		6.590	6520	1.355×10^{-4}	0.863	1.333×10^{-4}	0.859	5418	1.194×10^4
5 wt%		6.620	10045	8.51241×10^{-5}	0.876	7.8642×10^{-5}	0.894	6369	1.642×10^4
15 wt%		7.022	9379	9.181×10^{-5}	0.865	8.6935×10^{-5}	0.872	5976	1.536×10^4
316L	Chloride	8.57	3689	3.05×10^{-4}	0.81	3.182×10^{-4}	0.796	6091	9.788×10^3
0 wt%	+ thiosulfate	7.809	3999	2.333×10^{-4}	0.778	2.461×10^{-4}	0.771	8111	1.212×10^4
5 wt%		7.913	7515	8.783×10^{-5}	0.874	8.7908×10^{-5}	0.871	6562	1.408×10^4
15 wt%		8.447	6863	1.607×10^{-4}	0.8067	1.4275×10^{-4}	0.850	6548	1.342×10^4

0.002 mol/L Na₂S₂O₃ solutions are given in the same order as the capacitance ring radius and impedance modulus.

3.5. Mott-Schottky curve analysis

Mott-Schottky curve (M – S) analysis is a tool that is largely used to investigate the characteristics of passivation films. The semiconductor characteristics of passivation layers grown on W/HEA in 3.5 wt% NaCl plus 0.002 mol/L Na₂S₂O₃ solution were studied using M – S analysis.

When the concentration of the fluid in the spatial charge area of the hydrocarbonated film is exhausted by adjusting the extra voltage, the

capacitive (C) of the space charge area and the extra voltage (E) are supported in the Mott-Schottky baseline equation by Eqs. (3) and (4) [48].

$$\frac{1}{C^2} = \pm \frac{2}{\varepsilon \cdot \varepsilon_0 \cdot e \cdot N} \left(E - E_{FB} - \frac{KT}{e} \right) \quad (3)$$

$$N = \frac{2}{m \cdot e \cdot \varepsilon \cdot \varepsilon_0} \quad (4)$$

The relative dielectric constant of the semiconductor is denoted as ε . ε_0 is the vacuum transducer constant. e is an electron charge (1.60218×10^{-19} C). k is the Boltzmann constant, and T is the absolute temperature. The carrier density is divided into two categories: electrocatalytic

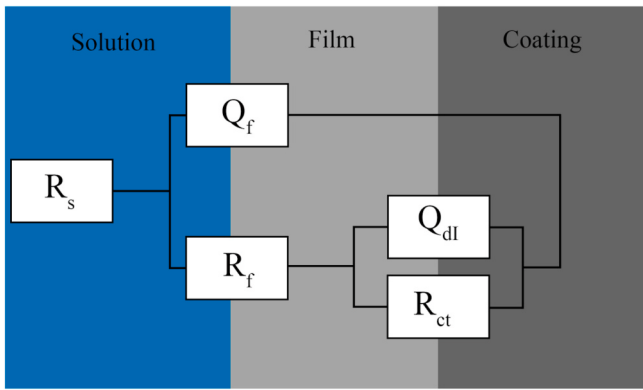


Fig. 9. The equivalent circuit of the EIS diagram.

density (N_A) is an n-type semiconductor, and receptor density (N_D) is a p-type semiconducting. E applies power to the electrode. E_{FB} is flat-band power. m is the inclination of the Mott-Schottky plots in the linear region. The positive slope represents the n-type semiconductor properties, and the negative slope indicates the p-types. Fig. 10 shows Mott-Schottky plots of passive films for 316L substrate and HEA/ W_x ($x = 0, 5$, and 15 wt\%) specimens in $3.5 \text{ wt\%}/\text{L NaCl}$ plus $0.002 \text{ mol/L NaS}_2\text{O}_3$ solution. The two distinct linear regions of the semiconductor characteristics of p-types and n-types are displayed from 0 to -0.6 V and 0 – 0.6 V , respectively. In general, aluminium oxide and iron oxide/hydroxide, the main products of passive film, have the characteristics of n-type semiconductors. Chromium oxide, which is also the main oxide in the non-source membrane, possesses the characteristics of p-type semiconductors [52]. Based on the results of the Mott-Schottky curve, the characteristics of the p-n junction are presented on the HEA/ W_x ($x = 0, 5$, and 15 wt\%) samples and the 316L substrate. The larger the curve inclination, the lower the defect density in the passive film and the better the corrosion resistance. The curve inclination of the passive film formed in $3.5 \text{ wt\%}/\text{L NaCl}$ plus $0.002 \text{ mol/L NaS}_2\text{O}_3$ solution is in the range of 5 wt\% specimen $> 15 \text{ wt\%}$ specimen $> 316\text{L}$ substrate $> 0 \text{ wt\%}$ specimen. The greater the curve inclination, the more likely the passive film will be presented with a smaller defect density, indicating better corrosion resistance. Song et al. [53] discovered that AlCoCrFeNi2.1 eutectic high-entropy alloys, when combined with Ce elements, affect the slope of the curve and increase the defect density of the formed passive films. In this study, a small quantity of W-doped HEA coatings reduced the defect density of the passivation film formed in $3.5 \text{ wt\%}/\text{L NaCl}$ plus $0.002 \text{ mol/L NaS}_2\text{O}_3$ solution.

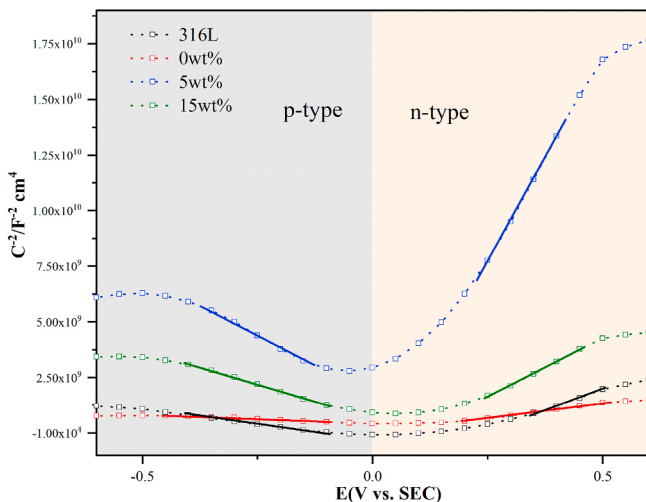


Fig. 10. M – S plots of passive films for 316L substrate and HEA/ W_x ($x = 0, 5$, and 15 wt\%) specimens in $3.5 \text{ wt\%}/\text{L NaCl}$ plus $0.002 \text{ mol/L NaS}_2\text{O}_3$ solution.

NaCl plus $0.002 \text{ mol/L NaS}_2\text{O}_3$ solution.

3.6. XPS analysis

The XPS technique was employed to evaluate the surface passivation films to determine the chemical organization and composition of the passive films of HEA/ W_x coatings. Metal Co^0 , Co_3O_4 , Co(OH)_2 , and satellite peaks contribute to several corners of the $\text{Co}2\text{p}3/2$ spectrum, as shown in Fig. 11(a). The corrosion resistance of the passive film is little affected by the Co element. The metals Al^0 and Al_2O_3 exhibit a couple of peaks in the $\text{Al}2\text{p}$ spectrum. Al_2O_3 can positively influence corrosion resistance (see Fig. 11(b)). The $\text{Fe}2\text{p}3/2$ spectrum has been defined by combining metallic Fe^0 and Fe_2O_3 peaks (see Fig. 11(c)). The spectrum of $\text{W}4\text{f}$ is provided in Fig. 11(d), where two peaks are identified in the range of 33.6 eV and 37.7 eV , established by WO_3 . In addition, peaks corresponding to the W element have been identified in 29.2 eV and 33.2 eV created for metal W^0 . The $\text{Ni}2\text{p}3/2$ spectrum (see Fig. 11(e)) indicates the peaks of metallic Ni^0 and Ni(OH)_2 . The metallic form is the primary Ni species present, and Ni has a lower capacity to oxidize than other elements. The $\text{Cr}2\text{p}3/2$ spectra were decomposed into two distinctive peaks for the metals Cr^0 and Cr_2O_3 , as seen in Fig. 11(f). Cr_2O_3 can prevent iron dissolution, increasing stainless steel passivation protection. A couple of peaks of the $\text{O}1\text{s}$ (see Fig. 11(g)) spectra for O^{2-} and OH^- represent the hydrated oxide species characterized by M-OH . The two peaks of the $\text{O}1\text{s}$ (see Fig. 11(g)) spectrum for O^{2-} and OH^- show the M-OH characteristic of the hydrated oxide species. It is the result of an anhydrous oxide species, $\text{M}-\text{O}$ (M is an alloying element). A couple of the $\text{S}2\text{p}$ (see Fig. 11(h)) spectrum for SO_3^{2-} and SO_4^{2-} suggest that most of the sulfur-forming compounds are engaged in forming the oxide film and adsorbed on the surface of the oxide film. The XPS study demonstrated that the passive film on the surface of the HEA/ W_x ($x = 0, 5$, and 15 wt\%) coatings consisted of Al_2O_3 , Cr_2O_3 , Fe_2O_3 , Ni(OH)_2 , Co_3O_4 , Co(OH)_2 , and WO_3 . Ni has the strongest signal among all metallic state elements, followed by Co . Since the electronic configuration of Ni and Co has filled d orbitals, making it more difficult to oxidize compared to the incompletely filled d orbitals of the elements, the oxidation kinetics of nickel and cobalt are lower than those of chromium, tungsten and aluminium [51]. Passivation film emerges, while WO_3 , Cr_2O_3 , Fe_2O_3 and Al_2O_3 forms on a surface. WO_3 increases the density of the passivation film in a chloride solution with thiosulfate. The formation of Cr_2O_3 , Al_2O_3 , Fe_2O_3 , and WO_3 is attributed to the reactions of Eqs. (5)–(8) [33,35].



3.7. Immersion corrosion experiment

To study the corrosion morphology of HEA/ W_x ($x = 0, 5$, and 15 wt\%) specimens in chloride solution with thiosulfate, the HEA/ W_x specimens were immersed in $3.5 \text{ wt\%}/\text{L NaCl}$ plus $0.002 \text{ mol/L NaS}_2\text{O}_3$ solution for 1000 h to explore the local corrosion behavior of HEA/ W_x coatings.

Fig. 12 shows the surface morphology of HEA/ W_x ($x = 0, 5$, and 15 wt\%) specimens. It is found that there is no presence of thermal cracks on the surface of the 0 wt\% specimen (see Fig. 12(a)). The crevice defects are present in the 5 wt\% and 15 wt\% specimens, as shown in Fig. 12 (b and c). Due to the thermal expansion coefficient mismatch between the coatings and the substrate, coatings inside can generate tensile stresses, which are converted into residual stresses to generate hot cracks [54]. Previous studies [55] found that residual compressive

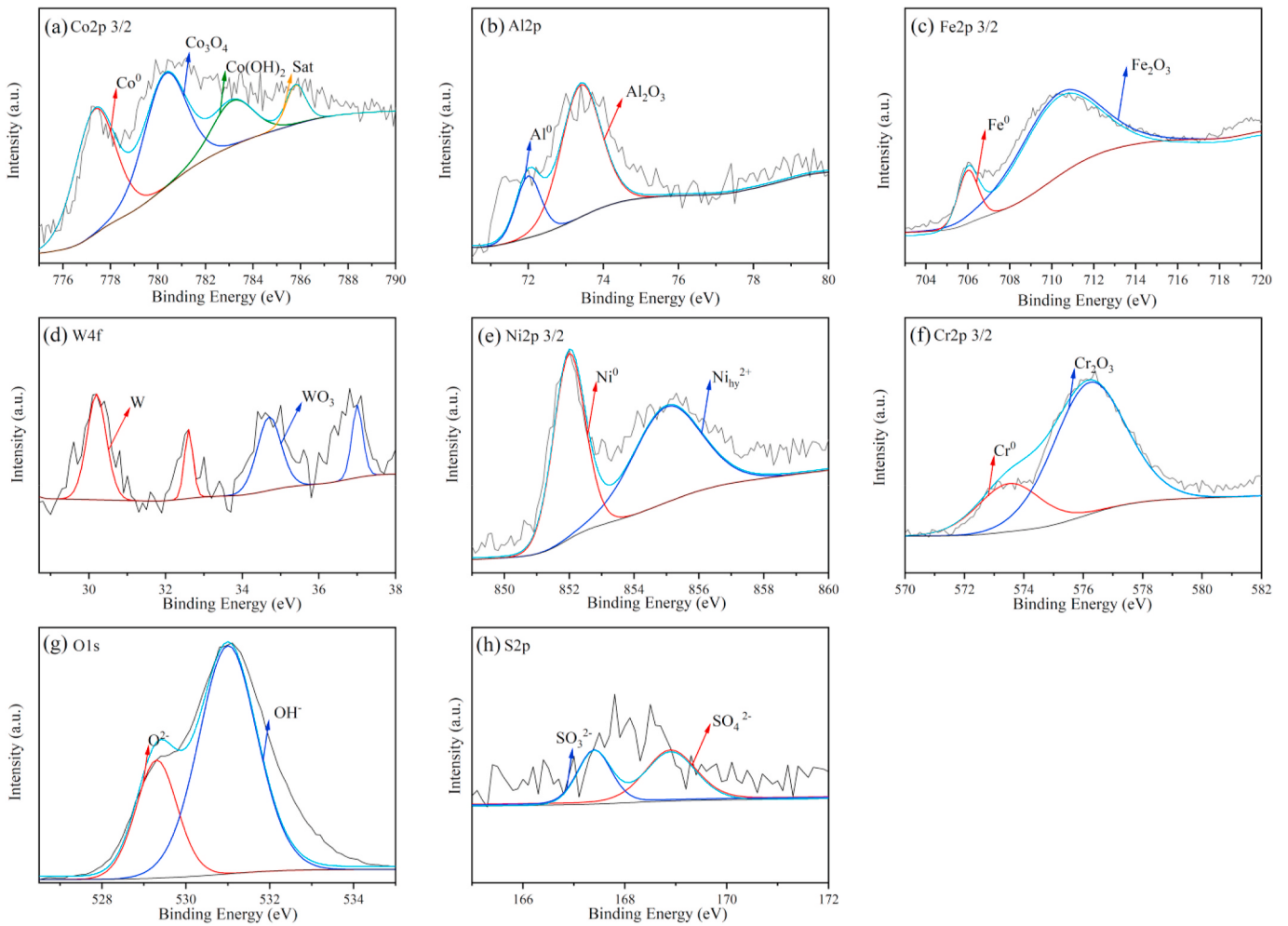


Fig. 11. XPS spectra of passive films for HEA/W_x ($x = 0, 5$, and 15 wt%) specimens in 3.5 wt%/ L NaCl plus 0.002 mol/ L NaS_2O_3 solution. (a) $\text{Co}2\text{p}$; (b) $\text{Al}2\text{p}$; (c) $\text{Fe}2\text{p}$; (e) $\text{Ni}2\text{p}$; (f) $\text{Cr}2\text{p}$; (g) $\text{O}1\text{s}$; (h) $\text{S}2\text{p}$.

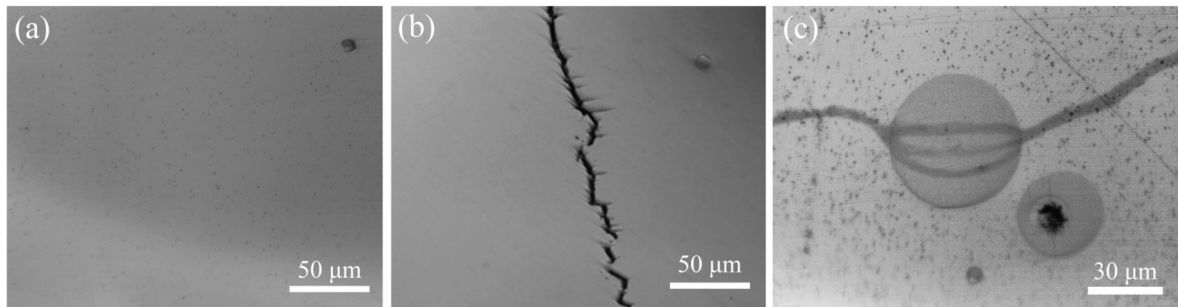


Fig. 12. The OM image of coatings of HEA/W_x ($x = 0, 5$, and 15 wt%) specimens before being immersed. (a) 0 wt% specimen; (b) 5 wt% specimen; (c) 15 wt% specimen.

stresses are caused by the combined effect of thermal and translation stresses in the coating, while residual tensile stresses at the layer-substrate interface cause breaks that arise and develop perpendicular to the surface. The corrosion morphology of HEA/W_x ($x = 0, 5$, and 15 wt%) specimens immersed in a chloride solution containing sulfide for 1000 h (see Fig. 13). It can be found that intergranular corrosion (IGC) was caused by the stacked corrosion products on the coatings, and short LGC defects were expanded to form long LGC defects (see Fig. 13(a-b), (d-e)). Intergranular corrosion and fracture surfaces between surface and spherical W particles (see Fig. 13(g and h)). Mondou et al. [56] investigated the effect of the sensitivity of the grain

boundary for IGC on exposure conditions and a larger chloride ion concentration in the electrolyte captured within the IGC defects when transforming from short to long IGC defects. The fracture surface formed was shown after demonstrating intergranular corrosion expansion on the coating surface, as shown in Fig. 13(c). A small amount of corrosion products, fractures, and microcracks were found around the crevices (see Fig. 13(f-i)). Following 1000 h of immersion, the corrosion morphology results indicate that, among the HEA/W_x coatings, the 5 wt % W-doped HEA coating has a greater resistance to localized corrosion, which provides some protection against intergranular corrosion. The regions labeled LC₁, LC₂, LC₃, LC₄, and LC₅ on the surface of the 5 wt %

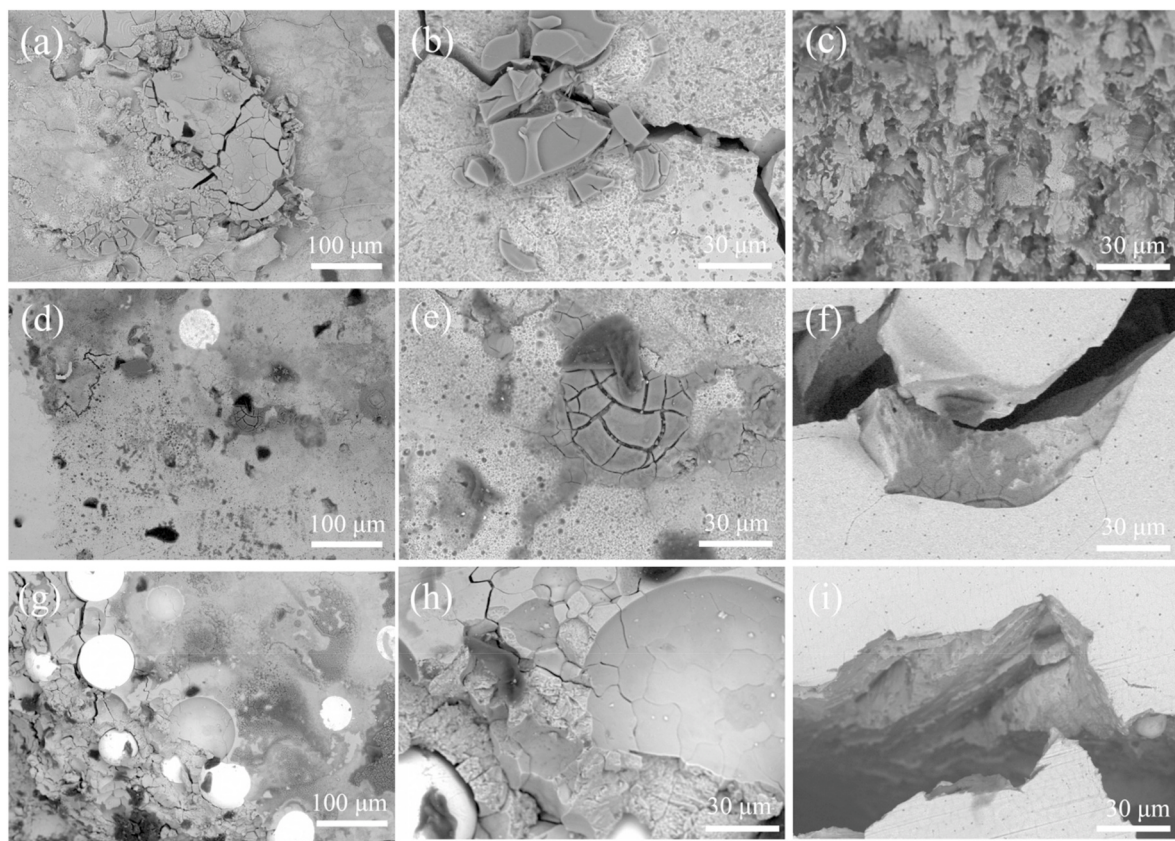


Fig. 13. The SEM image of the corrosion morphology of HEA/W_x ($x = 0, 5$, and 15 wt%) specimens immersed for 1000 h in 3.5 wt%/L NaCl plus 0.002 mol/L NaS₂O₃ solution. (a–c) 0 wt% specimen; (d–f) 5 wt% specimen; (g–i) 15 wt% specimen.

specimen immersed in a chloride solution containing thiosulfate for 1000 h are the local corrosion products, which are shown in Fig. 14. For the purposes of further assessing the corrosion products, line EDX technology was used (see Fig. 15) to analyze the LC₁–LC₅ areas and find out how the corrosion products were distributed in terms of elements on the coating's surface. In Fig. 15, the chlorine (Cl), sulfur (S), and oxygen (O) elements in the LC₁ and LC₃–LC₅ regions show a clear distribution trend and peak. This shows that the main way that sulfides, oxides, and chlorides are made is by oxygen, sulfur, and chlorine reacting with coating surfaces. The coating surface's PH value will gradually drop as a

result of the buildup of corrosion products [57,58], which causes grain boundary fissures to open up and eventually result in intergranular corrosion and long IGC defects. The crack gaps were at the 388 – 452 μm position, and no elemental distribution was detected after line EDX technology, as shown in Fig. 15. However, an identical pattern of S and Ni peak change was discovered near the crevice fractures, suggesting that surface S and Ni elements in the region have a combination. Previous papers [59,60] found that S and Ni elements combine to generate sulfide on the metal's surface, and this adsorption results in the formation of a sulfide (M_xS_y) on the coating's surface. It is clear that the peak

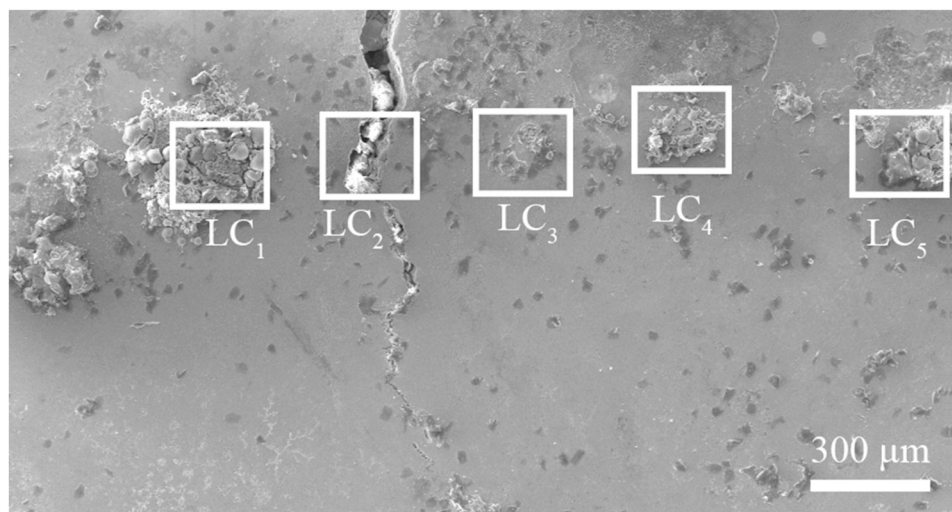


Fig. 14. Distribution diagram of corrosion products of the 5 wt% specimen immersed for 1000 h in 3.5 wt%/L NaCl plus 0.002 mol/L NaS₂O₃ solution.

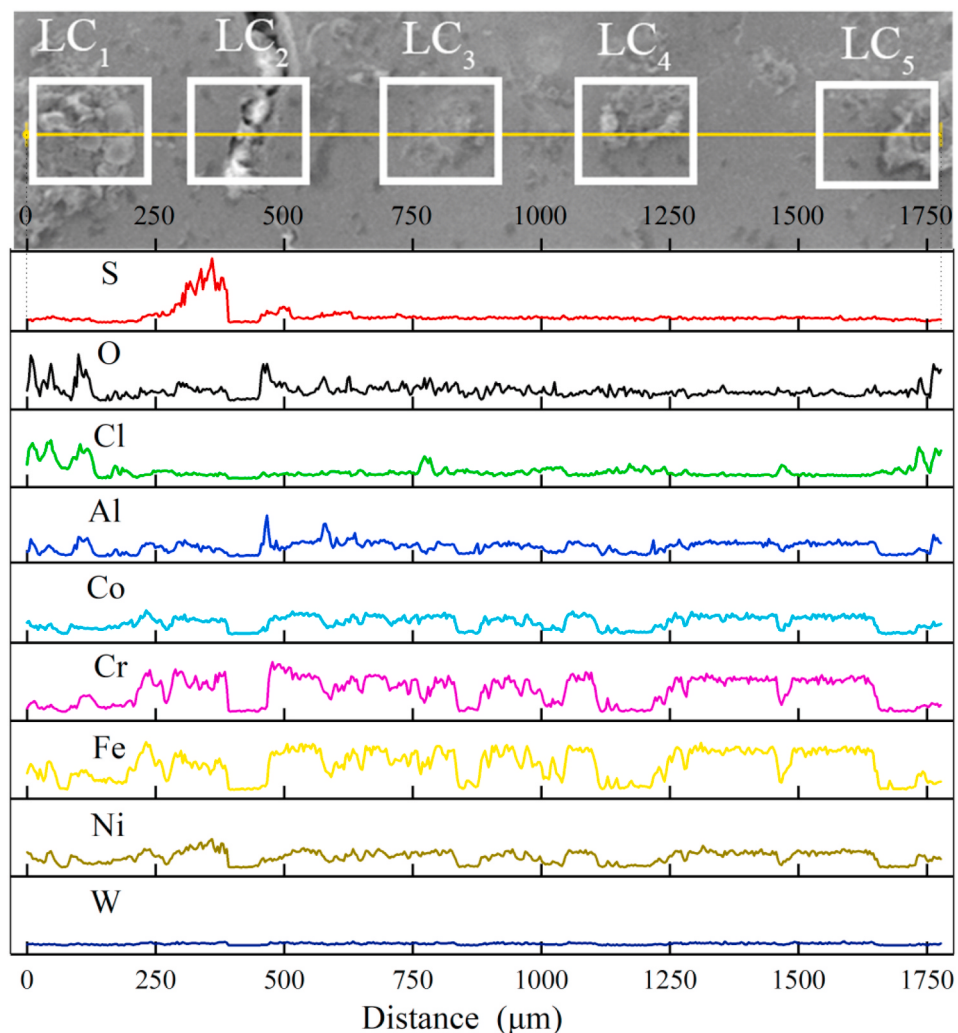


Fig. 15. Line EDX analysis of the elemental distribution of corrosion products of the 5 wt% specimen immersed for 1000 h in 3.5 wt%/L NaCl plus 0.002 mol/L Na₂S₂O₃ solution.

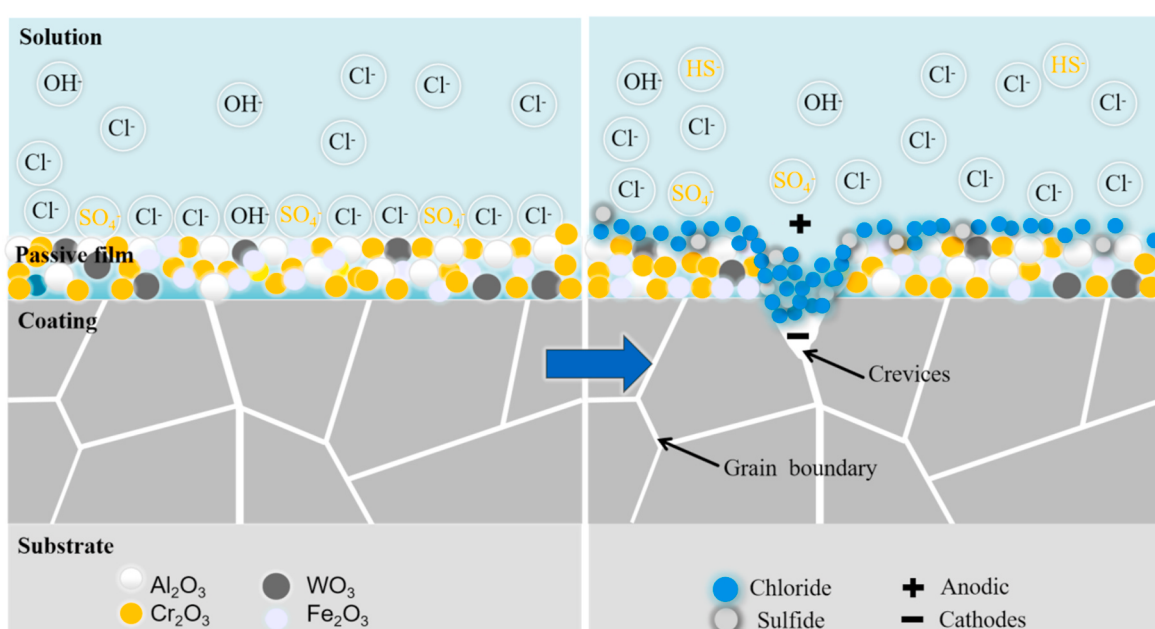
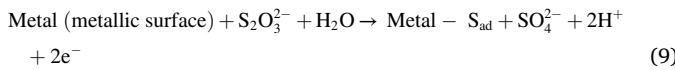


Fig. 16. Schematic diagram of the mechanism of dissolution of the passive film of localized corrosion in 3.5 wt%/L NaCl plus 0.002 mol/L Na₂S₂O₃ solution.

values of Al, Cr, and O elements in the LC₂ region change from 450 to 700 μm. This suggests that the reaction between these elements in this region creates a Cr-Al-rich passive film [61].

3.8. Mechanisms of dissolution and localized corrosion of passivation films

According to the passive film mechanism schematic diagram (see Fig. 16), Cr₂O₃, Al₂O₃, Fe₂O₃, and WO₃ concentration generates a passivation film. The chloride and sulfide form a competitive adsorption relationship, with sulfide buildup impeding the passive film's repair. The reactions that occur for sulfide are described in Eq. (9) [62].



Eq. (10) [62] explains sulfide growth with the time of chemical reaction with W-doped HEA coatings.



Chloride ions decompose the passivation film and form chlorides. Sulfides and chlorides are enriched and accumulate at grain boundaries, absorbing oxygen ions and increasing the cathodic potential. The large number of cations in the external solution shows a positive pole, gradually forming crevices (IGC defect). The nearly depleted oxygen ions in the closed crevices indicate a cathode, producing a protocell effect and accelerating the local corrosion rate [63].

4. Conclusions

Several methods were used to evaluate the corrosion behavior of HEA/W_x (x = 0, 5, and 15 wt%) coatings in a simulated sulfur-containing seawater environment. The main conclusions are summarized as follows.

- (1) The XRD, EDS, and EDX measurements verify that the primary phases of the HEA coatings are the Cr-Fe-rich A2 phase and the Al-Ni-rich B2 phase. The addition of W-doped HEA coatings modifies the ratio of the A2 phase to the B2 phase but does not substantially alter the ΔS_{mix} and microhardness. W-doped HEA coatings may improve corrosion resistance by changing the A2 to B2 phase ratios.
- (2) The electrochemical impedance spectra (EIS) and potentiodynamic polarization curve analysis demonstrate that the 5 wt% W-doped HEA coating in a simulated sulfur-containing seawater environment can strengthen the resistance to localized corrosion and exhibit greater corrosion resistance and denser passivation film, as evidenced by a higher self-corrosion potential (E_{corr}), a lower corrosion current density (i_{corr}), and a lower passivation current density (i_p), as well as a higher negative phase angle, a higher polarization resistance (R_p), and a higher impedance modulus ($|Z|$).
- (3) M – S and XPS techniques were used to explore the kinds and attributes of passivation films in HEA/W_x (x = 0, 5, and 15 wt%) coatings. The passivation films generated by HEA/W_x coatings are of the P-N semiconductor type. The defect density of the passivation films reduces while rising as W elements are doped into the HEA coatings. The 5 wt% W-doped HEA coating reduced the defect density in the passivation film. The passivation film of the HEA/W_x coatings mainly consists of Cr₂O₃, Al₂O₃, Fe₂O₃, and WO₃.
- (4) The corrosion morphology after 1000 h of immersion in a simulated sulfur-containing seawater environment. As the amount of W-doped in the HEA coating grows in simulated sulfur-containing seawater environment, the intergranular corrosion resistance of HEA/W_x coatings rises and then falls, as shown by the line EDX analysis. The 5 wt% W-doped HEA coating enhanced intergranular corrosion resistance, yet the 15 wt% W-doped HEA coating diminished it.

Funding

National Natural Science Foundation of China (No. 62073089); The Project of Postgraduate Demonstration Courses (No. 2023SFKC_041)

CRediT authorship contribution statement

Yang Zhao: Writing – original draft, Software, Data curation, Conceptualization. **Zhikai Zhu:** Methodology, Investigation. **Wenqing Shi:** Validation, Supervision, Software. **Jiang Huang:** Writing – review & editing.

Declaration of competing interest

The authors declared no potential conflicts of interest with respect to the research, authorship, and publication of this article.

Data availability

The data that has been used is confidential.

References

- [1] Shouxin Zhang, Jialin Yan, Long Zheng, Jinsheng Sun, Jianfeng Gao, Effect of alternating current and Cl⁻ ions on corrosion behavior of X70 steel in NaCl solution, *Int. J. Electrochim. Sci.* 18 (2023) 49–58.
- [2] Ming-Fei Shao, Tong Zhang, Herbert Han-Ping Fang, Xiangdong Li, The effect of nitrate concentration on sulfide-driven autotrophic denitrification in marine sediment, *Chemosphere* 83 (2011) 1–6.
- [3] Yul Sorokin, O.Yu Zakusina, Acid-labile sulfides in shallow marine bottom sediments: a review of the impact on ecosystems in the Azov Sea, the NE Black Sea shelf and NW Adriatic lagoons, *Estuarine, Coastal and Shelf Science* 98 (2012) 42–48.
- [4] Paul A.J. Lusty, The Oceans and massive sulfide deposits, in: David Alderton, Scott A. Elias (Eds.), *Encyclopedia of Geology*, second ed., Academic Press, 2021, pp. 978–992.
- [5] Nés T.E. Fonseca, M. José Feio, Ana Rosa Lino, M.A. Reis, Valter L. Rainha, The influence of the media on the corrosion of mild steel by Desulfovibrio desulfuricans bacteria: an electrochemical study, *Electrochim. Acta* 43 (1998) 213–222.
- [6] R. Liu, Y. Shan, S. Xi, X. Zhang, C. Sun, A deep-sea sulfate-reducing bacterium generates zero-valent sulfur via metabolizing thiosulfate, *mLife* 1 (2022) 257–271.
- [7] Marko Stipanicev, Florin Turcu, Loic Esnault, Elmar Werner Schweitzer, Renate Kilian, Régine Basseguy, Corrosion behavior of carbon steel in presence of sulfate-reducing bacteria in seawater environment, *Electrochim. Acta* 113 (2013) 390–406.
- [8] Lokesha Macdonald Choudhary, D. Digby, Akram Alfantazi, Role of thiosulfate in the corrosion of steels: a review, *Corrosion* 71 (2015) 1147–1168.
- [9] R.C. Newman, W.P. Wong, H. Ezuber, A. Garner Garner, Pitting of stainless steels by thiosulfate ions, *Corrosion* 45 (1989) 282–287.
- [10] Ao Ni, Han Zhang, Huihui Xu, Shengchuan Wu, Dong Liu, Pingguang Xu, Yuhua Su, Qianhua Kan, Guozheng Kang, Corrosion fatigue crack growth behavior of a structurally gradient steel for high-speed railway axles, *Eng. Fract. Mech.* 281 (2023) 109166.
- [11] Sihan Lu, Qingchuan Wang, Yi Zhang, Huabing Li, Hao Feng, Lili Tan, Ke Yang, A novel biodegradable high nitrogen iron alloy with simultaneous enhancement of corrosion rate and local corrosion resistance, *J. Mater. Sci. Technol.* 152 (2023) 94–99.
- [12] Haijia Huang, Chen Jia, Ou Zhao, Lanhai Guo, Local corrosion morphology analysis and simplification of low carbon steel plates, *Ocean Eng.* 268 (2023) 113372.
- [13] J.W. Yeh, S.K. Chen, S.J. Lin, J.Y. Gan, T.S. Chin, T.T. Shun, Nanostructured high-entropy alloys with multiple principal elements: novel alloy design concepts and Outcomes, *Adv. Eng. Mater.* 6 (2004) 299–303.
- [14] B. Cantor, I.T.H. Chang, P. Knight, A.J.B. Vincent, Microstructural development in equiatomic multicomponent alloys, *Mater. Sci. Eng.* 375–377 (2004) 213–218.
- [15] Yacheng Fang PanMa, Shuimiao Wei, Zhiyu Zhang, Hong Yang, Shiguang Wan, Konda Gokuldoss Prashanth, Yandong Jia, Microstructure and mechanical properties of AlCoCrFeMnNi HEA fabricated by selective laser melting, *J. Mater. Res. Technol.* 25 (2023) 7090–7100.
- [16] Z. Mohamed Lamiaa, Ayman H. Elsayed, Omayma A. Elkady, Shimaa A. Abolkassem, Physico-mechanical, microstructure, and chemical properties of Si/Ti/Nb additions to CoCrMoW medium entropy alloys, *J. Mater. Res. Technol.* 24 (2023) 9897–9914.

- [17] Syam Narayana Addepalli, Sharnappa Joladarashi, M.R. Ramesh, Phase evolution and high-temperature wear behavior of non-equiautomic metastable CoCrNiTiMox HEA coatings fabricated by high-velocity oxy-fuel technique, *Mater. Today Commun.*, 35 (2023) 106310.
- [18] Junyan Wang, Xiufang Cui, Guo Jin, Yao Zhao, Xin Wen, Ye Zhang, Effect of in-situ Ni interlayer on the microstructure and corrosion resistance of underwater wet 316L stainless steel laser cladding layer, *Surf. Coating. Technol.* 458 (2023) 129341.
- [19] Zia Ullah Arif, Muhammad Yasir Khalid, Ans Al Rashid, Ehtsham ur Rehman, Muhammad Atif, Laser deposition of high-entropy alloys: a comprehensive review, *Opt. Laser. Technol.* 145 (2022) 107447.
- [20] Hui Liang, Dongxu Qiao, Junwei Miao, Zhiqiang Cao, Hui Jiang, Tongmin Wang, Anomalous microstructure and tribological evaluation of AlCrFeNiW0.2Ti0.5 high-entropy alloy coating manufactured by laser cladding in seawater, *J. Mater. Sci. Technol.* 35 (2021) 224–234.
- [21] Zia Ullah Arif, Muhammad Yasir Khalid, Ehtsham ur Rehman, Sibghat Ullah, Muhammad Atif, Ali Tariq, A review on laser cladding of high-entropy alloys, their recent trends and potential applications, *J. Manuf. Process.* 68 (2021) 225–273.
- [22] Yan Xiao, Chengdong Sun, Xiongyu Wu, Xiaofan Zhu, Yajing Kan, Yan Zhang, Restoration of pure copper motor commutator for aviation by laser powder deposition, *J. Mater. Res. Technol.* 23 (2023) 5796–5806.
- [23] Ping Zhang, Ziwei Li, Haomin Liu, Yuabin Zhang, Huaixue Li, Chuanwei Shi, Peng Liu, Dongfang Yan, Recent progress on the microstructure and properties of high entropy alloy coatings prepared by laser processing technology: a review, *J. Manuf. Process.* 76 (2022) 397–411.
- [24] Xiaojian Shang, Zonglun Wang, Xianghai Wu, Qibin Liu, Yaxiong Guo, Kailu Ding, Tianhai Liao, Laser cladding [Cr-Fe4Co4Ni4]Cr2.6-xAlxMo0.4 high-entropy alloy coating to strong-acid erosion, *Intermetallics* 156 (2023) 107847.
- [25] Chao Qi, Tingting Guo, Tom Jarvis, Xinhua Wu, Peter Hodgson, Daniel Fabijanic, Direct laser deposition cladding of AlxCrFeNi high entropy alloys on a high-temperature stainless steel, *Surf. Coating. Technol.* 332 (2017) 440–451.
- [26] Mohammad Fereidouni, Mahmoud Sarkari Khorrami, Mahmoud Heydarzadeh Sohi, Liquid phase cladding of AlxCrFeNi high entropy alloys on AISI 304L stainless steel, *Surf. Coating. Technol.* 402 (2020) 126331.
- [27] S.S. Liu, M. Zhang, G.L. Zhao, X.H. Wang, J.F. Wang, Microstructure and properties of ceramic particle reinforced FeCoNiCrMnTi high entropy alloy laser cladding coating, *Intermetallics* 140 (2022) 107402.
- [28] Shudan Li, Defu Liu, Guan Liu, Siwei Xin, Zixin Deng, Chunye Li, Tao Chen, Study on the preparation of CeO₂-doped AlCoCrFeNiTi high entropy alloy bioinert coatings by laser cladding: the effect of CeO₂ particle size on the tribological properties of the coatings, *Surf. Coating. Technol.* 475 (2023) 130155.
- [29] Jing Dai, Hao Feng, Hua-Bing Li, Hong-Chun Zhu, Shu-Cai Zhang, Jin-Dong Qu, He Tong, Zhou-Hua Jiang, Tao Zhang, Insights into the mechanism of Mo protecting CoCrFeNi HEA from pitting corrosion—a quantitative modelling study on passivation and repassivation processes, *J. Mater. Sci. Technol.* 182 (2024) 152–164.
- [30] Jia-li Zhou, Yan-hai Cheng, Yi-xing Wan, Hao Chen, Yun-fei Wang, Jin-yong Yang, Strengthening by Ti, Nb, and Zr doping on microstructure, mechanical, tribological, and corrosion properties of CoCrFeNi high-entropy alloys, *J. Alloys Compd.* (2024) 173819.
- [31] Caiyun Shang, Eugen Axinte, Jun Sun, Xuting Li, Peng Li, Jianwei Du, Pengchao Qiao, Yan Wang, CoCrFeNi(W1-xMox) high-entropy alloy coatings with excellent mechanical properties and corrosion resistance prepared by mechanical alloying and hot pressing sintering, *Mater. Des.* 117 (2017) 193–202.
- [32] Zekun Wang, Jian Zhu, Yongming Guo, Wuhong Xin, Xidong Hui, Yongling Wu, Hongyu Zheng, Yang Zhao, Xiaoming Wang, Multi-effects of Mo on enhancement of wear and corrosion resistances of FeCoNiCrMox high entropy alloys coatings prepared by laser powder directed energy deposition, *Surf. Coating. Technol.* 477 (2024) 130378.
- [33] Mengjiao Li, Qingjun Chen, Xia Cui, Xinyuan Peng, Guosheng Huang, Evaluation of corrosion resistance of the single-phase light refractory high entropy alloy TiCrVNb0.5Al0.5 in chloride environment, *J. Alloys Compd.* 857 (2021) 158278.
- [34] Jianming Wang, Hui Jiang, Wenlong Xie, Xiao Kong, Shengxue Qin, Hongwei Yao, Yong Li, Effect of Mo addition on microstructural evolution and corrosion behaviors of AlCrFeNi3 eutectic high-entropy alloy, *Corrosion Sci.* 229 (2024) 111879.
- [35] Ziyi Zhou, Lin Wang, Xiaohua Zhao, Jili Wu, Feng Zhang, Jinhong Pi, Effects of W addition on the corrosion behaviors of FeCoNiCrMn high entropy alloy composites in the 3.5 wt.% NaCl solution, *Surface. Interfac.* 23 (2021) 100956.
- [36] Zuozhe Niu, Juan Xu, Tao Wang, Nairan Wang, Zihan Han, Yan Wang, Microstructure, mechanical properties and corrosion resistance of CoCrFeNiW_x (x = 0, 0.2, 0.5) high entropy alloys, *Intermetallics* 112 (2019) 106550.
- [37] Yang Gao, Haibo Xiao, Bin Liu, Yong Liu, Enhanced drilling performance of impregnated diamond bits by introducing a novel HEA binder phase, *Int. J. Refract. Metals Hard Mater.* 118 (2024) 106449.
- [38] G.J. Zhang, Q.W. Tian, K.X. Yin, S.Q. Niu, M.H. Wu, W.W. Wang, Y.N. Wang, J. C. Huang, Effect of Fe on microstructure and properties of AlCoCrFexNi (x=1.5, 2.5) high entropy alloy coatings prepared by laser cladding, *Intermetallics* 119 (2020) 106722.
- [39] Zeyu Hu, Li Yang, Bingwen Lu, Na Tan, Lanrong Cai, Qingsong Yong, Effect of WC content on microstructure and properties of high-speed laser cladding Ni-based coating, *Opt. Laser. Technol.* 155 (2022) 108449.
- [40] Yunfeng Li, Yan Shi, Guangjun Jiang, Shufeng Tang, Jianxin Wu, Jiasheng Wang, Effect of WC on microstructure, molten pool and properties of Ni based coatings by multi-layer laser cladding, *Opt. Laser. Technol.* 174 (2024) 110612.
- [41] Q.-Y. Wang, Y.-C. Xi, Y.-H. Zhao, S. Liu, S.-L. Bai, Z.-D. Liu, Effects of laser remelting and annealing on microstructure, mechanical property and corrosion resistance of Fe-based amorphous/crystalline composite coating, *Mater. Char.* 127 (2017) 239–247.
- [42] Zhaotong Li, Cainian Jing, Yan Feng, Zhonglin Wu, Tao Lin, Jingrui Zhao, Phase evolution and properties of AlxCoCrFeNi high-entropy alloys coatings by laser cladding, *Mater. Today Commun.* 35 (2023) 105800.
- [43] Zhen Zhang, Xiaofeng Li, Hong Yi, Huiqi Xie, Zhan Yong Zhao, Peikang Bai, Clarify the role of Nb alloying on passive film and corrosion behavior of CoCrFeMnNi high entropy alloy fabricated by laser powder bed fusion, *Corrosion Sci.* 224 (2023) 111510.
- [44] A. Nicolas, Andrea Nicolas, A.W. Mello, Alberto W. Mello, M.D. Sangid, Michael D. Sangid, The effect of strain localization on galvanic corrosion pitting in AA7050, *Corrosion* 74 (2018) 1366–1378.
- [45] Yang Zhong, Yu Mei, Chao Han, Zhenjiang Zhao, Xuejiao Jia, Mingyu Zhao, Songmei Li, Jianhua Liu, Evolution and corrosion resistance of passive film with polarization potential on Ti-5Al-5Mo-5V-1Fe-1Cr alloy in simulated marine environments, *Corrosion Sci.* 221 (2023) 111334.
- [46] R.G. Kelly, R.G. Kelly, The importance of local chemistry and potential in localized corrosion and stress corrosion cracking, *Corrosion* 78 (2022) 114–126.
- [47] D.H. Xia, S.Z. Song, J.Q. Wang, J.L. Luo, Research progress on sulfur-induced corrosion of alloys 690 and 800 in high temperature and high pressure water, *Acta Metall. Sin.* 53 (2017) 1541–1554.
- [48] T. Gancarz, K. Mech, J. Guspil, K. Berent, Corrosion studies of Li, Na and Si doped Zn-Al alloy immersed in NaCl solutions, *J. Alloys Compd.* 767 (2018) 1225–1237.
- [49] Longfei Song, Hu Wenbin, Bokai Liao, Wan Shan, Lei Kang, Xingpeng Guo, Corrosion behavior of AlCoCrFeNi2.1 eutectic high-entropy alloy in Cl-containing solution, *J. Alloys Compd.* 938 (2023) 168609.
- [50] Jiantao Zhang, Xiaojun Hu, Kuochih Chou, Effect of thiosulfate on corrosion behavior and passive films of duplex stainless steel 2205 in chloride solutions, *Int. J. Electrochem. Sci.* 14 (2019) 9960–9973.
- [51] Xin-Hui Gu, Xin-Ran Li, Qin-Hao Zhang, Lian-Kui Wu, Fa-He Cao, Passive film and surface characterization of Alx(CoCrFeNi)100-x (x = 0, 5, 10, 15, 20) high entropy alloys, *Intermetallics* 162 (2023) 107994.
- [52] Jiantao Zhang, Xiaojun Hu, Kuochih Chou, Effect of thiosulfate on corrosion behavior and passive films of duplex stainless steel 2205 in chloride solutions, *Int. J. Electrochem. Sci.* 14 (2019) 9960–9973.
- [53] Longfei Song, Wenbin Hu, Shiyu Huang, Xingpeng Guo, Electrochemical behavior and passive film properties of Ce-added AlCoCrFeNi2.1 eutectic high-entropy alloys in sulfuric acid solution, *J. Electroanal. Chem.* 950 (2023) 117883.
- [54] Ivan Gnesin, Boris Gnesin, Aleksei Nekrasov, Ways to reduce the negative consequences of the thermal expansion coefficient mismatch of a carbon-carbon composite and a protective silicide coating, *J. Alloys Compd.* 767 (2018) 803–810.
- [55] Yulei Feng, Kai Feng, Yueqiao Feng, Zhuguo Li, Influence of residual stress on the cracking of the laser-cladded high-hardness coating, *Mater. Lett.* 349 (2023) 134715.
- [56] Emilie Mondou, Arnaud Proietti, Cédric Charvillat, Cyril Berziou, Xavier Feaugas, David Sinopoli, Christine Blanc, Understanding the mechanisms of intergranular corrosion in 2024 Al alloy at the polycrystal scale, *Corrosion Sci.* 221 (2023) 111338.
- [57] B. Gwinner, C. Bataillon, R. Chelagendib, N. Gruet, V. Lorentz, B. Puga, Effect of the oxidizing power of the medium on intergranular corrosion of AISI 310 SS: influence of diffusion, *Electrochim. Acta* 470 (2023) 143334.
- [58] Yuexing Liang, Guoai Li, Li Liu, Jiantang Jiang, Jian Cao, Wenzhu Shao, Zhen Liang, Corrosion behavior of Al-6.8Zn-2.2Mg-Sc-Zr alloy with high resistance to intergranular corrosion, *J. Mater. Res. Technol.* 24 (2023) 7552–7569.
- [59] Peng Zhang, Zhou Xu, Zhongping Yao, Yanyan Liu, Shouyuan Lin, Mingyu He, Songtao Lu, Xiaohong Wu, A high-corrosion-resistant high-entropy alloys (HEAs) coatings with single BCC solid solution structure by laser remelting, *Mater. Lett.* 324 (2022) 132728.
- [60] A.A. Becerra, M.A. Rodríguez, M.A. Kappes, R.M. Carranza, Effect of thiosulfate on pitting corrosion of Ni-Cr-Fe Alloys in chloride solutions, *Corrosion* 74 (2018) 1214–1228.
- [61] Heon-Young Ha, Kyeong-Won Kim, Seong-Jun Park, Chang-Hoon Lee, Tae-Ho Lee, Hyun-Uk Hong, Joonoh Moon, A comparative study on passive films of Fe-11Cr stainless steel and Fe-20Mn-11.5Al-1.4C-5Cr lightweight steel, *J. Mater. Res. Technol.* 26 (2023) 6135–6145.
- [62] C. Duret-Thual, D. Costa, W.P. Yang, P. Marcus, The role of thiosulfates in the pitting corrosion of Fe-17Cr alloys in neutral chloride solution: electrochemical and XPS study, *Corrosion Sci.* 39 (1997) 913–933.
- [63] Heng Liu, Cunao Feng, Zening Wang, Yi Zhang, Dekun Zhang, Yu Yan, Study of fretting-initiated crevice corrosion and crevice corrosion affected fretting of stainless steel, *Corrosion Sci.* 225 (2023) 111586.